PAPER

Check for updates

Diesel soot oxidation over Mn–Pr–Ce oxide catalysts: structural changes and the impact of Mn doping

Sunaina S. Patil, [ID] [a] Hari Prasad Dasari, [ID] *[a] Rahulkumar Shirasangi[a] and Harshini Dasari [ID] *[b]

The soot oxidation activity of manganese-doped ceria-praseodymium catalysts, synthesized *via* solution combustion synthesis, was evaluated. The analyses performed with XRD and Raman spectroscopy indicated that the Mn-doped CP catalysts displayed the typical fluorite structure of CeO_2. The addition of Mn to CP led to a reduction in crystallite size from 14 nm to below 10 nm. The F_{2g} Raman active mode of fluorite-structured Ce and the oxygen vacancies resulting from the addition of Mn and Pr (bands ~ 560 cm^{-1} to 580 cm^{-1}) were consistently observed across all Mn-doped CP catalysts. 15 and 20 Mn-CP exhibited an additional secondary phase identified as Mn_2O_3. The analysis of BET surface area and BJH pore size revealed that the Mn-doped CP catalysts exhibited both micro and mesoporous characteristics. The H_2-TPR and O_2-TPD profiles indicated enhanced reducibility resulting from the incorporation of Mn and Pr into CeO_2-doped catalysts. The improved T_{50} (365 ± 1 °C) for the 5 Mn-CP catalytic system is primarily due to its increased specific surface area of 45 m^2 g^{-1} and the presence of active surface adsorbed oxygen species identified in the XPS and O_2-TPD studies. 5 Mn-CP exhibited the lowest activation energy value compared to all other Mn-doped catalysts.

1. Introduction

Regenerating diesel particulate filters (DPFs) in the automotive industry is difficult and expensive since they use a lot of energy and operate at high temperatures (around 800 °C). A pressure drop develops when the diesel engine's exhaust flow is restricted due to a clogged or blocked DPF, which could lead to additional engine damage. Therefore, it is important to regenerate the filter carefully so that no harmful byproducts are released, and all particulates should be contained within the constraints of particle size restrictions and the engine's life.[1]

Catalytic oxidation is the main technique used to reduce soot emissions. Adding catalysts lowers the oxidation temperature, whereas soot oxidizes at temperatures above 600 °C without catalysts.[2–5] Ce-based mixed oxides are promising catalysts for redox processes, particularly in soot oxidation.[6–14] The descriptors for Ce-based metal oxides that enhance the catalytic performance include the redox ability, the host structure, lattice oxygen species,

site isolation, the nature of the metal–oxygen bond, multifunctionality, and phase cooperation.[15] They are also known as the seven pillars, which regulate the activity based on the different reaction conditions. Additional criteria for better catalytic activity may include great oxygen storage capacity (OSC), porosity, and high surface area.[16]

Shuang *et al.*[17] identified the parameters affecting activity and stability. The ceria-based catalysts oxidize soot *via* a Mars–van Krevelen mechanism, wherein gaseous O_2 initially adsorbs onto Ce, dissociates into atomic O and then converts into Ox species. CeO_2, whether utilized as a catalyst or as a support in the passive regeneration of particulate filters, is likely of minimal significance due to its inadequate textural stability under high-temperature reactions often present in exhaust gases. Upon exposure to elevated temperatures, the surface area of CeO_2 significantly diminishes, concurrently resulting in the potential loss of its redox characteristics and oxygen storage capacity. The modification of CeO_2 with diverse ions is recognized to enhance stability against sintering and augment the oxidation activity of the resultant catalysts. This alteration was ascribed to the variations in redox characteristics and the formation of oxygen vacancies, both enhancing oxygen exchange with the catalyst and increasing oxygen storage capacity.[18] Some literature indicates that a positive correlation between catalytic performance and specific surface area is not assured.[17,19] Instead, the catalytic soot

[a] *Energy and Catalysis Materials Laboratory, Chemical Engineering Department, National Institute of Technology Karnataka, Surathkal, Mangalore-575025, Karnataka, India. E-mail: energyhari@nitk.edu.in; Tel: +91-8242473610*

[b] *Chemical Engineering Department, Manipal Institute of Technology Manipal Academy of Higher Education, Manipal, 576104, Udupi, Karnataka, India. E-mail: harshini.dasari@manipal.edu; Tel: +91-8202924316*

oxidation depends on the interaction efficiency between active sites and soot on the surface.[20] Rare earth and transition metals were doped with Ce to address sintering and thermal stability difficulties.[7,21,22] In addition to Ce, the rare earth elements consist of praseodymium (Pr), terbium (Tb), dysprosium (Dy), lanthanum (La), gadolinium (Gd), samarium (Sm), neodymium (Nd), europium (Eu), scandium (Sc), yttrium (Y) and so on.[6,7,23–27] Among them, La, Pr, Nd, Sm, Gd, and Tb were tested for soot oxidation activity, and most of them displayed significantly enhanced catalytic activity.[6–9,28–35] It has been identified that ceria modified with La- and particularly Pr- remains highly effective as a thermally stable catalyst.[6,18]

Pr appears to exert a promotional effect on the catalytic behavior of ceria, potentially linked to the reducibility of PrO_x.[6,18,36] Praseodymium oxide exhibits the highest redox capability and promptly reduces adsorbed neutral dioxygen (O_2) to the inert lattice oxide anion (O^{2-}).[36] Pr has larger ionic radii than Ce and is quickly reducible; Pr also exhibits a multioxidation state, which may improve its characteristics and reduce the temperature required for soot combustion.[7]

Additionally, transition metals such as chromium (Cr), iron (Ir), manganese (Mn), copper (Cu), cobalt (Co), hafnia (Hf), and zirconia (Zr) are chosen as dopants because most of them can exist in multiple oxidation states.[21,37] Among them, Mn is one of the most accessible transition metals, with numerous applications.[38] Liang et al.[39] indicated that CuCe, followed by MnCe mixed oxides, are the most effective catalysts. In a loose contact mode, MnCe demonstrates the most remarkable activity, regardless of the presence of NOx.[6,39] Mn's popularity in catalysis arises mostly from its multiple oxidation states.[40] Research indicates that manganese oxide-based catalysts exhibit superior performance in soot oxidation activity.[38,40–43] Mn has a substantially smaller ionic size than Ce and is easily reducible because it occurs in numerous valence states, passing on both extrinsic and intrinsic oxygen vacancies.[44] Mn, as a dopant, results in increased oxygen storage capacity (OSC) and thermal stability.[22,45] In the current study, the CeO_2 is modified by doping with Pr and Mn, which possess redox ability.

Catalytic preparation techniques are crucial to fine-tuning the shape and physicochemical characteristics. Ce-based catalysts and complex oxides are synthesized using coprecipitation,[46,47] hydrothermal,[48] solution combustion synthesis,[34,49,50] sol–gel,[51] microemulsion,[52] the EDTA-citrate method,[53,54] and solvothermal methods.[3,55] Among these, solution combustion synthesis (SCS) creates homogenous powders with high purity, which is a quick and straightforward procedure, saving time and energy.[56,57] In this study, Mn-doped CP catalysts ($Mn_{x(x=0–0.2)}(Ce_{0.9}Pr_{0.1})_{1-x}O_{2-\delta}$) with varying Mn concentrations were synthesized using the SCS method. The catalysts were characterized and tested for effectiveness towards soot oxidation.

2. Methodology

2.1. Synthesis methodology

The catalysts were synthesized *via* solution combustion synthesis (SCS). Metal nitrates [$Ce(NO_3)_3 \cdot 6H_2O$ (Sigma-Aldrich ≥99%), $Pr(NO_3)_3 \cdot 6H_2O$ (Sigma-Aldrich ≥99%), and $Mn(NO_3)_3 \cdot 6H_2O$ (Sigma-Aldrich ≥98%)] and glycine were well dissolved in distilled water, according to the stoichiometric ratio maintaining a glycine (fuel) to nitrate (oxidizer) mole ratio (G/N) of 0.35. The solution was heated and agitated continuously at 70 °C until it became a viscous gel. The gel is then transferred to a preheated (350 °C) oven, where it is auto-ignited, and the obtained voluminous powder is calcined at 600 °C/5 h to eliminate impurities. The $Mn_{x(x=0–0.2)}(Ce_{0.9}Pr_{0.1})_{1-x}O_{2-\delta}$ catalysts with various Mn concentrations (5, 10, 15, 20 mol%, keeping ceria-praseodymium (CP) constant) were prepared and are herein denoted as 5 to 20 Mn-CP and Mn oxide.

2.2. Characterization

The obtained catalysts are further characterized to determine the phase, structure, surface area, morphology, and occurrence of oxygen vacancies. The characterization tools such as X-ray diffraction (XRD) analysis (Malvern PAN analytical: Empyrean diffractometer, Kα radiation; λ = 1.54 Å), FT-Raman spectroscopy (LabRAM HR Horiba, France, Ex = 532 nm laser beam), BET surface area and BJH pore size analysis (Anton Paar-Autosorb iQ-XR-XR 195364 Quantachrome instruments), and X-ray photon spectroscopy (XPS) (Omicron ESCA+ – ultrahigh vacuum) were used in the present study. Before fitting the peaks for XPS, the baseline and carbon (C1s) peak correction (284.6 eV) were performed. The reducibility ratio and surface active oxygen species ratio were calculated by measuring the ratio of individual ions to total ions.

H_2-temperature programmed reduction (H_2-TPR) and O_2-temperature programmed desorption (O_2-TPD) analyses of the catalysts were carried out with a chemisorption analyzer (BELCAT-II, M/s Microtrac, Japan). For the O_2-TPD analysis, a 100 mg catalyst was pretreated at 300 °C/1 h in He and subsequently cooled to room temperature in He; the catalyst was then pretreated with a 5% O_2/He mixture (30 mL min^{-1}) at room temperature for 1 h. Following treatment in the oxidizing environment, the catalyst was heated from ambient temperature to 900 °C under He (30 mL min^{-1}) at 10 °C min^{-1}. For the H_2-TPR analysis, a 100 mg catalyst was pretreated from room temperature to 500 °C in 5% O_2/He at 10 °C min^{-1}, held at 500 °C/1 h in the same environment and subsequently cooled to room temperature in He, and then the catalyst was heated to 900 °C at 10 °C min^{-1} in 10% H_2/Ar gas mixture.

2.3. Soot oxidation activity

Soot oxidation reactions were performed in a Thermo Gravimetric Analyser (TGA, Exstar TGA/DTA 6300). Soot and catalyst (wt ratio of 1 : 10) were mixed using an electric agate mortar and pestle for 45 min. The heating rate for the oxidation reaction is maintained at 10 °C min^{-1} with a temperature range from room temperature to 600 °C with an airflow rate of 100 mL min^{-1} (atm. pressure). To determine activation energy (E_a), the heating rate (β) for the soot oxidation reaction in TGA was varied at 5, 10, 15, and 20 °C min^{-1}. The Flynn Wall Ozawa method[58] was employed to determine average activation energy, calculated from the

slope of $\log(\beta)$ *vs.* $1/T$ (K^{-1}) plots where 'T' refers to the temperature in Kelvin.

3. Results and discussion

3.1. Characterization of the developed catalysts

3.1.1. X-ray diffraction (XRD) analysis. The XRD spectra of $Mn_{x(x=0-0.2)}(Ce_{0.9}Pr_{0.1})_{1-x}O_{2-\delta}$ and pure Mn oxide catalysts (Fig. 1) show that the planes correspond to fluorite CeO_2 (JCPDS 01-075-0120).[50,51,59,60] No secondary diffraction peaks corresponding to pure Mn_2O_3 were observed in any doped catalyst samples.[48] The planes [(200), (211), (222), (321), (400), (332), (431), (440), and (622)] found for Mn-oxide conformed closely to the bixbyite crystal phase of Mn_2O_3 (JCPDS no. 41-1442).[61,62] No peaks linked with Pr oxides (PrO_2,[63] Pr_2O_3,[64] and Pr_6O_{11}[10]) were noted, and in general, they exhibit the essential peaks associated with the cubic fluorite structure, identical to CeO_2.

Table 1 shows the crystallite size (obtained using the Scherrer equation[65]), lattice strain, and facet ratios ({100}/{111} and {110}/{111}) for the catalysts. It was discovered that 20 Mn-CP had the smallest crystallite size and the largest lattice strain, measuring 5.67 nm and 0.0262, respectively. Pure Mn oxide exhibited a greater crystallite size and a lower lattice strain (30.04 nm and 0.0043, respectively). As per the previous investigations,[34] when Pr was added to CeO_2, the crystallite size reduced from 21 nm to 14 nm. The further addition of Mn to the CP catalyst system reduced the crystallite size from 14 nm to less than ~10 nm. Reactive facets are one of the most important characteristics in determining catalytic activity enhancement.[66] It has been demonstrated that ceria exhibiting a higher number of exposed planes from the {100} and {110} facets shows enhanced activity in comparison to those with a predominance of {111}.[67] Mn-loaded CP catalysts exhibit much higher lattice strain and facet ratios ({110/111}) than bare CP catalysts; hence, adding Mn to CP enhanced its physiochemical

properties, which could contribute to improved catalytic efficiency. The addition of Mn to Ce indicated a reduction in the crystallinity of the Ce–Mn catalysts. The doped Ceria catalysts exhibited broad/wider diffraction peaks without any obvious shift, indicating MnOx in a well-dispersed phase.[53,68]

3.1.2. Raman spectroscopy. Raman spectra of $Mn_{x(x=0-0.2)}(Ce_{0.9}Pr_{0.1})_{1-x}O_{2-\delta}$ catalysts are shown in Fig. 2. The peak at ~465 cm^{-1} in all doped samples is ascribed to the active F_{2g} Raman modes of CeO_2, indicating a symmetric arrangement of O–Ce–O.[7,29,44,51] The peak at ~560 cm^{-1} is attributable to oxygen vacancies (O_v).[34,51] According to earlier investigations,[34] this peak was observed with the inclusion of Pr but not in pure CeO_2, suggesting that incorporating Pr enhances the presence of oxygen vacancies. Similarly to the XRD examination, no significant shift in the F_{2g} peak was seen in Mn-doped samples and no characteristic peaks of Pr oxides[69,70] were noticed in the spectra. Pure Mn oxide exhibits two strong peaks at 306 cm^{-1} (v_5 mode) and 643 cm^{-1} (v_1 mode) from Mn_2O_3, indicating asymmetric and symmetric Mn–O–Mn stretching.[71,72] The secondary phase appeared when the concentration of Mn-doping increased by 10 mol%. Mn-doped CP catalysts showed secondary v_1 mode peaks blended with existing O_v peaks for 15 and 20 Mn-CP catalysts. The $I_{O_v}/I_{F_{2g}}$ values indicate the oxygen vacancy concentration in the catalysts, as measured by the Raman deconvolution of the O_v and F_{2g} peaks.[73] The intensity ratios ($I_{O_v}/I_{F_{2g}}$) of oxygen vacancy peaks to the characteristic F_{2g} of Ce were computed for all doped samples and are shown in Table 1. The findings indicated that the $I_{O_v}/I_{F_{2g}}$ values were almost identical yet exhibited a decline with the rising Mn content; notably, the 10 Mn-CP displayed a merely elevated value of 0.78. This ratio typically serves to signify the population of oxygen vacancies or defects, which suggests a greater potential for enhanced catalytic reactivity.[74] Thus, it suggests that a reduced concentration of Mn dopant is advantageous for improving oxygen vacancies, which is then impacted by the presence of the secondary phase of Mn.

3.1.3. BET and BJH pore size analysis. The BET surface area (S_A), average pore size distribution, and pore volume are reported in Table 1. The table shows that the surface area ranged primarily between 20 and 45 m^2 g^{-1}. 5 Mn-CP had the greatest S_A of 45 m^2 g^{-1} among Mn-loaded CP catalysts. CP had the largest average pore size of 11.46 nm, whereas 15 Mn-CP had the highest total pore volume of 0.333 cc g^{-1}. Fig. 3(a) and (b) shows the N_2 adsorption–desorption isotherm and pore size distribution for the $Mn_{x(x=0-0.2)}(Ce_{0.9}Pr_{0.1})_{1-x}O_{2-\delta}$ catalysts.

Fig. 3(a) indicates that for Mn-doped CP catalysts, 5 Mn-CP and 20 Mn-CP exhibited identical Type IV isotherms with H4 hysteresis and minimal adsorption. Mn Oxide and 10 Mn-CP also demonstrated Type IV isotherms with H3 and H2 hysteresis, respectively. They display strong N_2 adsorption; in contrast, 10 Mn-CP displays delayed desorption. When the pore type exhibits a pore size smaller than the critical size of the adsorbent, cavitation occurs in the larger region, leading to increased challenges in fluid release from the pore during the desorption process, and such materials exhibit H2 hysteresis characteristics.[75] In contrast, materials exhibiting nonrigid
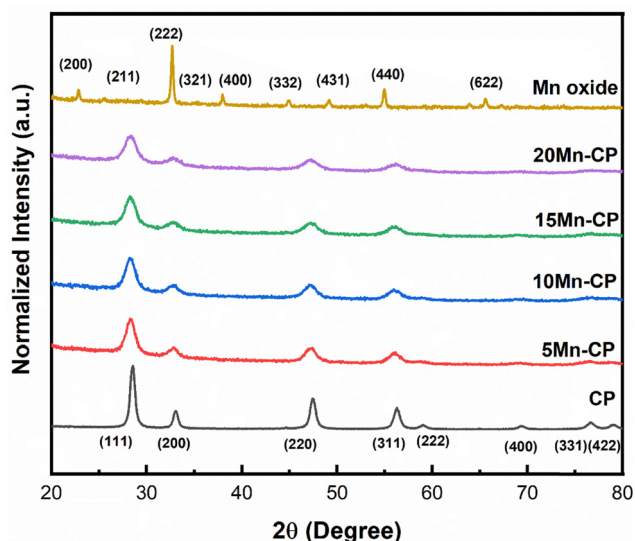

Fig. 1 XRD spectra of $Mn_{x(x=0-0.2)}(Ce_{0.9}Pr_{0.1})_{1-x}O_{2-\delta}$ catalysts synthesised by SCS, calcined at 600 °C/5 h.

Table 1 Physicochemical properties of the $Mn_{x(x=0-0.2)}(Ce_{0.9}Pr_{0.1})_{1-x}O_{2-\delta}$ catalysts from XRD and Raman spectroscopy and BET analysis

| Sample | Crystallite size (nm) | Lattice strain (ε) | Facet ratio | | $I_{O_V}/I_{F_{2g}}$ | BET S_A (m² g⁻¹) | Pore volume (cc g⁻¹) | Avg. pore size (nm) |
			{110}/{111}	{100}/{111}				
CP	14	0.0107	0.24	0.38	0.77	31	0.217	11.46
5 Mn-CP	07	0.0218	0.35	0.37	0.75	45	0.110	4.92
10 Mn-CP	07	0.0220	0.37	0.38	0.78	36	0.109	6.39
15 Mn-CP	06	0.0234	0.39	0.36	0.57	33	0.333	5.92
20 Mn-CP	06	0.0262	0.40	0.38	0.60	35	0.118	6.94
Mn	30	0.0043	—	—	—	20	0.039	4.08

aggregates, slit-shaped or plate-like pores that show unlimited absorption (at elevated P/P_o levels) are categorized under type H3 hysteresis. H4 hysteresis loops are commonly observed in intricate materials with micropores and mesopores.[75] Multiple loops in the 15 Mn CP type IV isotherms resulted in a step-wise isotherm associated with non-existing pores filled in a sub-step to genuine pores.[76] The pore size distributions of the Mn-doped catalysts were computed using the BJH method from the absorption isotherm curves, as shown in Fig. 3(b). All produced catalysts showed a narrow pore size distribution from 5 to 20 nm. Yang *et al.*[77] found that the produced Mn_2O_3 had a spongy nature and was extremely porous, with a large surface area, resulting in improved catalytic activity. Atmuri *et al.*[22,53] synthesized a series of Ce materials doped with varying mol% of Mn, ranging from 0 to 100. The surface area for Mn-doped Ce varied between 12 and 50 m² g⁻¹. Mn_3O_4 exhibited a minimal surface area of 12 m² g⁻¹, while the samples with 5 mol% Mn and 60 mol% Mn-doped Ce demonstrated a significantly higher

surface area of 50 m² g⁻¹. A linear correlation can be established between surface area and activity for BET surface areas less than 25 m² g⁻¹, regarded as a threshold for surface area.[6]

According to Krishna *et al.*,[18] the BET surface area of CeO_2 primarily originates from the micropores, which is difficult for soot particles to penetrate. The incorporation of rare-earth metals enhanced the meso/macro pore volume and the external surface area of CeO_2.[18]
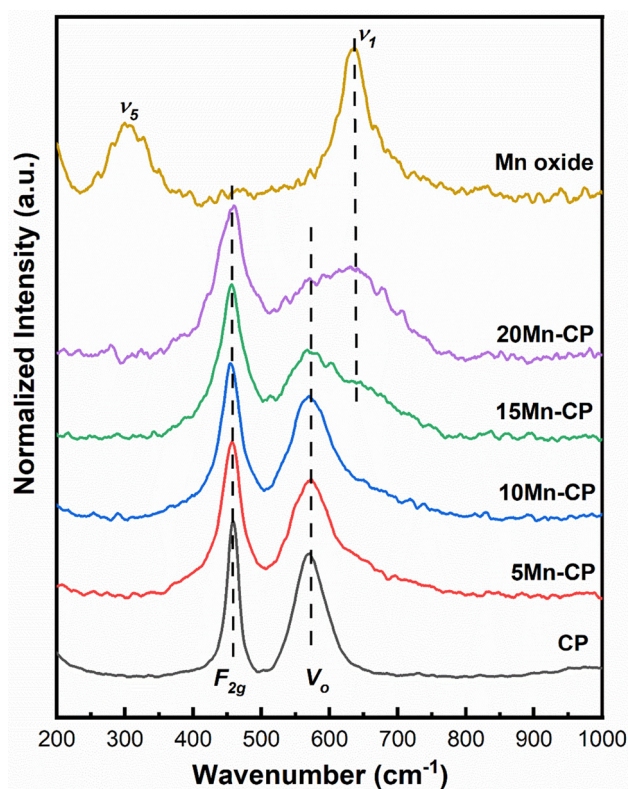
Fig. 2 Raman spectra of $Mn_{x(x=0-0.2)}(Ce_{0.9}Pr_{0.1})_{1-x}O_{2-\delta}$ catalysts.
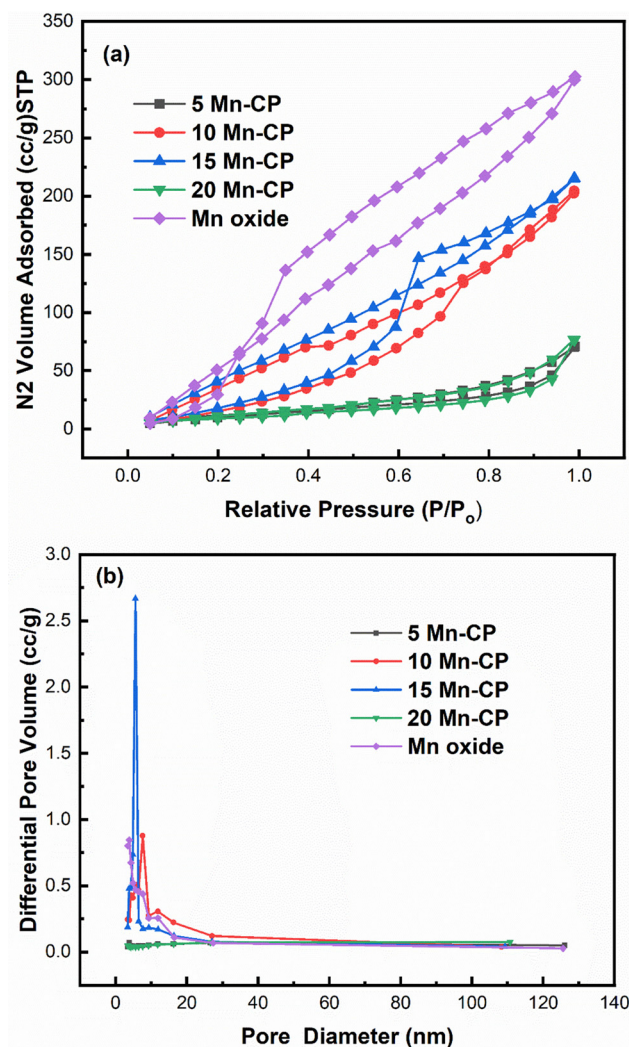
Fig. 3 (a) Adsorption–desorption isotherm; (b) BJH pore size distribution of $Mn_{x(x=0-0.2)}(Ce_{0.9}Pr_{0.1})_{1-x}O_{2-\delta}$ catalysts.
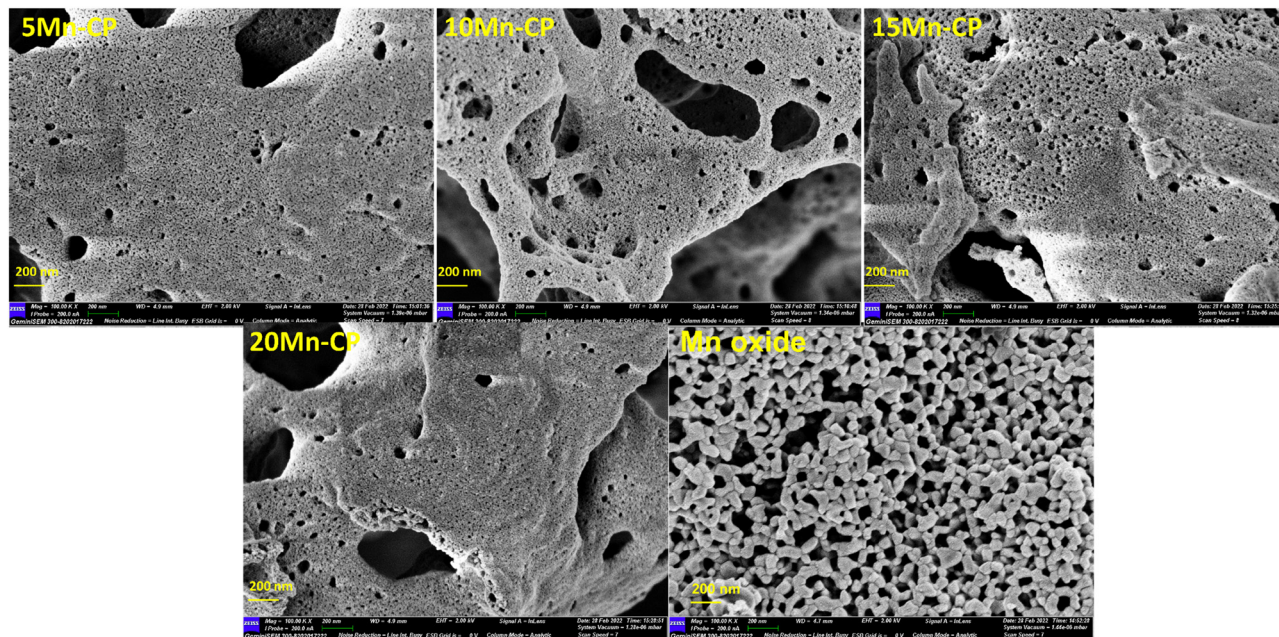
Fig. 4   FE-SEM analysis of $Mn_{x(x=0-0.2)}(Ce_{0.9}Pr_{0.1})_{1-x}O_{2-\delta}$ catalysts (200 nm).

3.1.4. FE-SEM analysis. Fig. 4 shows FE-SEM images of $Mn_{x(x=0-0.2)}(Ce_{0.9}Pr_{0.1})_{1-x}O_{2-\delta}$ and pure Mn oxide catalysts at 200 nm scale. Mn-doped CP catalysts exhibited a porous character when produced using the SCS approach.[78] It can be noticed that the particle size tends to increase as the Mn doping concentration is raised and porosity decreases. Pure Mn oxide displays different morphology and resembles a network of particles. The porous nature of the sample is crucial as it increases the active contact locations between soot and the catalyst.[79]

3.2. Redox property of the catalysts

3.2.1. XPS analysis. XPS spectra (Ce 3d, Pr 3d, O1s, and Mn 2p) for $Mn_{x(x=0-0.2)}(Ce_{0.9}Pr_{0.1})_{1-x}O_{2-\delta}$ catalysts are illustrated in Fig. 5(a)–(d). The Ce 3d spectrum (Fig. 5a) is categorized into two groups corresponding to the $3d_{3/2}$ and $3d_{5/2}$ orbitals.[41,80] According to Hassan et al.[81] the peaks defined as u^o, u, u', u'', and u''' at binding energy values $\sim$898.3, 900.4–901.9, 903.5, 907.3, and 916.3, correspond to the $3d_{3/2}$ spin–orbit states, while v^o, v, v', v'', and v''' at binding energy values 880.5, 882.0–883.9, 885.7, 888.7 and 898.0, respectively, correspond to the $3d_{5/2}$. The peaks at 880.5, 885.7, 898.3, and 903.5 are attributed to Ce^{3+}, while the remaining peaks are associated with Ce^{4+}. The peak positions attributed to the oxidation states Ce^{4+} and Ce^{3+} have been assigned based on reported literature.[41,80,82–84] Correspondingly, the deconvoluted XPS peaks for Pr 3d, O1s and Mn 2p were also designated.[48,71,81,85–91] It was reported by Paunović et al.[88] that, unlike the Ce 3d spectra, the Pr 3d spectra lack a precise and consistent mechanism for quantitatively analysing oxidation states using spectral deconvolution.[88] The binding energy of the $3d_{5/2}$ peak for PrO_2 is located between 933.2 and 933.9 eV. The peak position for Pr_2O_3 markedly deviates from the anticipated peak position of the PrO_2 compound, where the $3d_{5/2}$ XPS

peak is projected to occur between 935 and 936 eV.[87,88] For Pr_6O_{11}, the prominent peaks with binding energies of 933 eV for Pr $3d_{5/2}$ are indicative of Pr^{3+}, while the additional two peaks are ascribed to Pr^{4+} (935 eV) and a shake-off satellite (930 eV).[88] The second envelope at 950–970 eV pertains to emissions from Pr $3d_{3/2}$, whereas the last envelope at roughly 975 eV corresponds to the OKLL oxygen Auger peak.[86,92]

The presence of surface oxygen species is crucial for improving catalytic efficiency in soot oxidation reactions. The O1s spectra reveal the information corresponding to the lattice oxygen (O_L) species and the surface-adsorbed oxygen species (O_{Ads}).[90,91,93] From the O1s spectra of Mn-CP catalysts (Fig. 5c), the lattice oxygen peak was seen around 528.3 eV in CP and 5 and 10 Mn-CP; however, it shifted slightly to a lower binding energy of roughly 527.9 eV in the 15 and 20 Mn-CP.

The O1s spectra were analyzed for Co-doped transition metals such as Fe, Mn, and Cr, and the spectra were fitted into two distinct component peaks within the ranges of 529.7 to 531.5 eV (lattice oxygen) and 532.7 to 533.5 eV (surface adsorbed oxygen). O1s core level spectra of various ranges of Ce-based catalysts with dopants, including rare earth materials and transition metals, were studied by Mukherjee et al.[7] The peak identified at approximately 530.2 eV corresponds to lattice oxygen (O_α). In contrast, the peaks detected from 531.9 eV to 533.5 eV include adsorbed oxygen species, which comprise surface adsorbed oxygen (O_β), hydroxyls, chemisorbed water, and carbonates (O_λ).[7] Surface oxygen encompasses O_2^- (superoxide) and O_2^{2-} (peroxide) intermediates, which develop on the surface of CeO_2 when gaseous oxygen is gradually integrated into lattice oxygen.[7] Diez et al.[83] reported that the peak at lower binding energy (528.7 eV) is attributable to lattice oxygen, whereas the peak at higher binding energy (above 530 eV) is due to oxygen species formed by water interaction with the ceria surface.
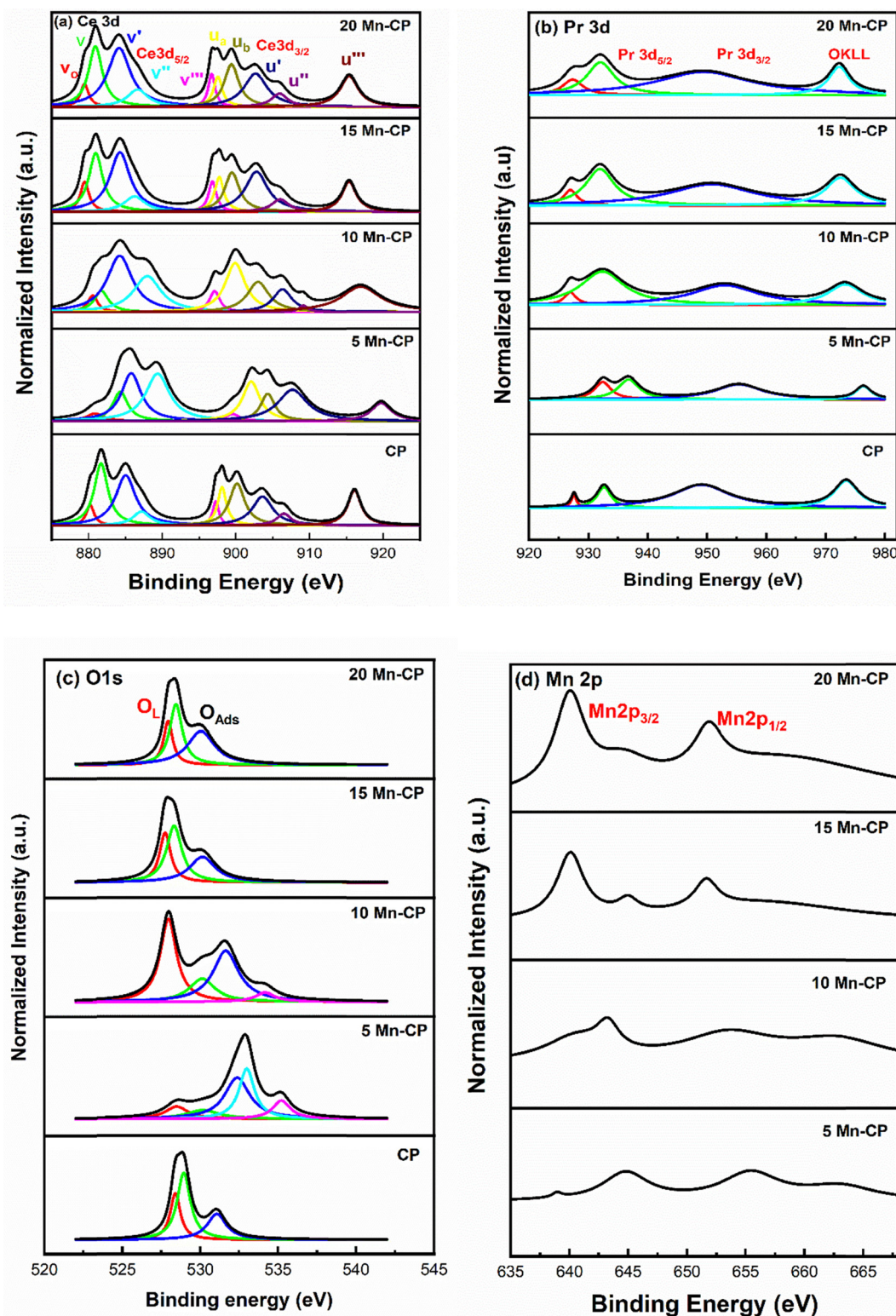
Fig. 5 (a) Ce 3d, (b) Pr 3d, (c) O1s and (d) Mn 2p XPS spectra for the $Mn_{x(x=0-0.2)}(Ce_{0.9}Pr_{0.1})_{1-x}O_{2-\delta}$ catalysts.

He et al.[94] indicated that the lattice oxygen species referred to as O^{2-} exhibit a peak at approximately 528.5 to 529 eV.[94,95] The other peaks are assigned as follows: surface adsorbed oxygen species O^- and O_2^- which is generally observed at 529.8 to 530.2 eV, the carbonates (CO_3^-) and hydroxyl species (OH^-) observed around 530.9–531.2 eV, and the latter peaks are dedicated as adsorbed molecular water (H–O–H). Fig. 5c shows that 5 Mn-CP and 10 Mn-CP showed the additional oxygen species at ∼534 eV, and the binding energy at 534 eV is assigned to the adsorbed H_2O or adsorbed molecular water.[96]

Li et al.[84] studied the O1s XPS spectra and demonstrated that the oxygen species are divided into six types. The Mn–Ce on carbon nanotube catalyst has binding energies of 529.6 and 530.3 eV, which correspond to the lattice oxygen of Ce–O and Mn–O, respectively. The peaks at 531.1 and 532.2 eV correspond to surface hydroxyls and adsorbed molecular water, respectively. The signal at 531.6 eV indicates a double bond between oxygen and carbon (C=O) from a carbonyl group, while the peak at 533.5 eV indicates a single bond. Paunović et al.[88] also investigated O1s peaks for Pr-doped CeO_2 samples and identified the peak corresponding to lower binding energy at 529.2 eV, while the peak associated with higher binding energy was found at 531.1 eV. With Pr doping, an increase in the higher binding energy peak was observed. Dimitrov et al.[97] indicated that the O1s chemical shift corresponds to the varying degree of ionicity in the M–O bonds. The reduction in binding energy in the XPS spectra of simple oxides can be attributed to an enhancement in the electron charge density of the oxide ions, resulting from an increase in their electronic polarizability.[97] Bonding an element to a different element causes a chemical change in its core levels compared to bonding with the same element. In metal oxides, metal atoms link with the more electronegative oxygen atom, resulting in greater binding energies at the core levels compared to the pure metallic state.[98] It was also indicated by Mukherjee et al.[7] that the lattice oxygen's surrounding environment in doped CeO_2 differs from the undoped one, which is attributed to the variation in electronegativity between the dopant and CeO_2. This leads to a variation in the peak position to varying degrees and in their study, the lattice oxygen peak of Ce–Mn had the lowest binding energy, demonstrating the existence of loosely bound lattice oxygen.[7]

The XPS spectra of Mn 2p (Fig. 5d) also consist of two groups, $2p_{1/2}$ and $2p_{3/2}$.[48,71] According to the literature, the Mn 2p spectra may be deconvoluted into four peaks at $\sim$ 642.35 eV and 643.70 eV (belonging to Mn $2p_{3/2}$), 653.95 eV, and 655.30 eV (refers to Mn $2p_{1/2}$). The peak observed at $\sim$ 660 eV is assigned as a satellite peak.[89,99] The binding energies of $Mn2p_{3/2}$ at 640.9, 641.8, and 642.5 for MnO, Mn_2O_3, and MnO_2, respectively, are too close to allow for a clear differentiation.[99] Even in the present spectra, the peaks of Mn species overlap, it is difficult to effectively differentiate the valence states and measure the Mn species.

The area under the curve was utilized to compute the reducibility ratio [$[Ce^{3+}/(Ce^{3+} + Ce^{4+})$; $Pr^{3+}/(Pr^{3+} + Pr^{4+})]$], and the surface oxygen species ratio listed in Table 2. The table shows that CP showed a high reducibility ratio for Ce^{3+} (0.42), and 5, 10 Mn-CP revealed a high concentration of Pr^{3+} (0.43) compared to all the Mn-doped catalysts. Thus, the presence of Pr contributed to the enhancement of Ce^{3+} species on the surface. Furthermore, doping with modest levels of Mn increased surface Pr^{3+} ions.

The ratios for lattice oxygen (O_L, 528.3 to 527.9 eV) and the surface adsorbed oxygen (O_{SAds}, 530.1 to 532.9 eV) along with adsorbed molecular water (H–O–H, 534.9 to 535.1 eV) are presented in Table 2. Adding Mn to Ce–Pr also significantly enhanced the concentration of surface oxygen species. It is observed that 10 Mn-CP exhibited the highest (0.39) lattice

Table 2 Reducibility ratio and surface oxygen species ratio of the $Mn_{x(x=0-0.2)}(Ce_{0.9}Pr_{0.1})_{1-x}O_{2-\delta}$ catalysts

Catalyst	Reducibility ratio (Ce^{3+} and Pr^{3+})		Lattice oxygen (O_L)	Adsorbed oxygen species (O_{Ads})	
	Ce^{3+}	Pr^{3+}	O_L	O_{SAds}	H–O–H
CP	0.42	0.15	0.26	0.74	—
5 Mn-CP	0.25	0.43	0.10	0.79	0.11
10 Mn-CP	0.39	0.43	0.39	0.56	0.05
15 Mn-CP	0.33	0.32	0.23	0.77	—
20 Mn-CP	0.32	0.30	0.27	0.73	—

oxygen (O_L) species, whereas 5 Mn-CP demonstrated a marginally greater quantity (0.79) of surface adsorbed oxygen species (O_{SAds}).

Generally, Ce-based catalysts express more than a single form of oxygen ion species,[100] and the active oxygen species obtained near binding energies of 530–532 eV play a critical role in oxidation reactions.[7,93,95] The surface-active oxygen species (O_2^{2-} and O^-) are also critical in improving catalytic activity at high temperatures[101] whereas the presence of lattice oxygen species (O^{2-}) plays a significant role in catalytic soot oxidation if the surface area is low.[16] In many instances, both oxygen species play a vital role in the soot oxidation reactions. However, the species that are adsorbed on the surface are actively involved in soot oxidation, and hence, a greater presence of surface-adsorbed oxygen suggests enhanced soot oxidation activity.[7]

3.2.2. H_2-temperature programmed reduction (TPR). The reducibility of the $Mn_{x(x=0-0.2)}(Ce_{0.9}Pr_{0.1})_{1-x}O_{2-\delta}$ catalysts was evaluated using H_2-TPR, as shown in Fig. 6. The reduction peak for CP was observed at 384 and 469 °C and a tiny additional peak at $\sim$ 548 °C, while the Mn-doped Ce–Pr catalysts showed peaks at 240 and 422 °C. The peak observed at temperatures lower than 450 °C was attributed to hydrogen consumption by oxygen species on catalyst surfaces, which is linked to catalytic performance.[102] The reduction peaks in CP are attributed to the main reduction of Pr^{4+} to Pr^{3+} (469 °C) and Ce^{4+} to Ce^{3+} (548 °C). The initial peak at 384 °C may be linked to the desorption or reduction of some surface invasion that the pre-treatment failed to remove, or to highly labile surface oxygen species.[103] The H_2-TPR profile reveals distinct peaks at 540 °C and 820 °C, indicating surface and bulk oxygen reduction processes in ceria, respectively,[104] and the latter $\sim$ 820 °C was too minimal and not significantly visible in the current study. The H_2-TPR spectrum of CeO_2 investigated by Chen et al.[102] displayed three reduction peaks at 382 °C, 510 °C, and 831 °C corresponding to the facile reduction of surface Ce^{4+} species, the surface reduction of capping oxygen within the lattice, and the reduction of bulk CeO_2 to Ce_2O_3.

For CeO_2, the low-temperature peak indicates the reduction of surface Ce^{4+} ions, and higher temperature contributes to the reduction of surface and lattice oxygen.[105,106] According to Mukherjee et al.,[7] CeO_2 reduction is anticipated to occur gradually. At temperatures below 527 °C, the outermost layers of Ce^{4+} undergo surface reduction, followed by bulk reduction at higher temperatures $\sim$ 777 °C. They discovered a low-
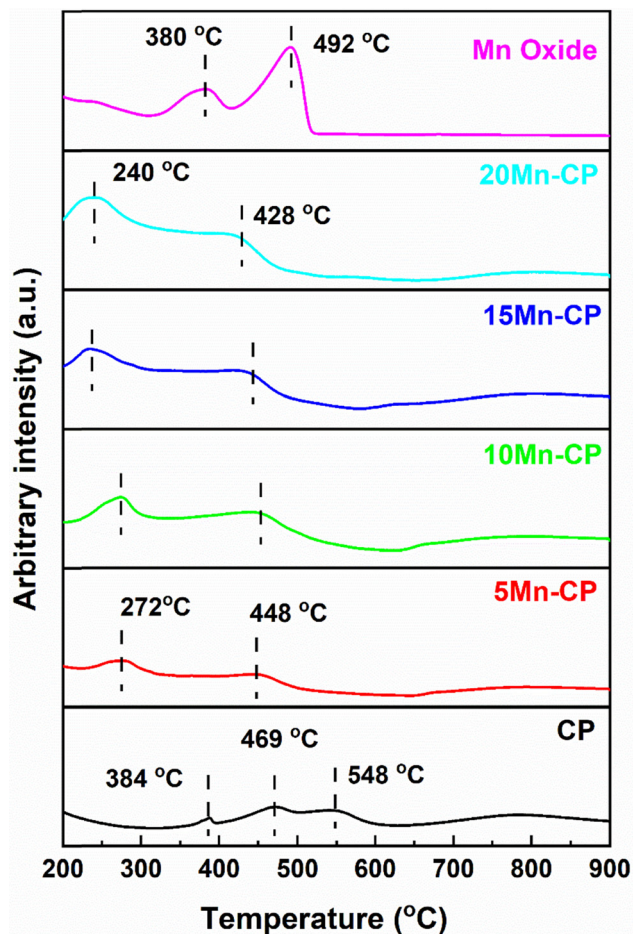
Fig. 6   H$_2$-TPR profiles of Mn$_{(x=5-20)}$(Ce$_{0.9}$Pr$_{0.1}$)O$_{2-\delta}$ catalysts.

temperature reduction pattern for Ce–Mn due to solid solution formation and interactions between Mn–O and Ce–O. This increases oxygen mobility from the bulk to the surface, resulting in greater sites on the surface for hydrogen adsorption.[7] Jan et al.[104] studied H$_2$-TPR analysis for pure CeO$_2$ and platinum-doped CeO$_2$ catalysts. Pure ceria demonstrates a two-step reduction process characterized by peaks at 540 °C and 820 °C, which are associated with the reduction of surface oxygen and bulk oxygen of ceria, respectively. Bulk oxygen exhibits a stronger bond with CeO$_2$ than surface oxygen; thus, it reacts with H$_2$ at very high temperatures. The reactant hydrogen gas is adsorbed onto platinum, which transfers the

adsorbed hydrogen to the surface of cerium oxide, thereby promoting the reduction of oxygen.[104]

Mn$_2$O$_3$ has two reduction peaks, first changing into Mn$_3$O$_4$ and then MnO. Typically. Mn$_2$O$_3$ shows a reduction peak at 288 and 385 °C. Zhang et al.[107] conducted H$_2$-TPR studies on α-, β-, γ-, and δ-MnO$_2$ catalysts. Gong et al.[108] found that α-Mn$_2$O$_3$ exhibited reduction peaks at 378 °C and 481 °C, while γ-Mn$_2$O$_3$ showed reduction at 367 °C and 466 °C. These peaks were consistent with the current study's findings for pure Mn oxide. The reduction peaks for CP (at 384 and 469 °C) shifted to lower temperatures for all Mn-doped CP catalysts, showing increased reduction capacity and oxygen species mobility. At lower temperatures, the active oxygen species increase and are reduced by H$_2$.[109] Hence, including Mn and Pr eases the reducibility and doping of Mn and Pr with Ce, allowing oxygen to circulate more freely. Table 3 presents the total hydrogen consumption at reduction peaks, and it can be seen that Mn oxide displays high consumption. For catalytic activity, the H$_2$ consumption at a reduction temperature below 450 °C is considered, and the order among doped catalysts is as follows: CP < 5 Mn-CP < 10 Mn-CP < 15 Mn-CP < 20 Mn-CP indicates that doping Mn and Pr facilitates the breakage of Ce–O.

3.2.3.   O$_2$-temperature programmed desorption (TPD). O$_2$-TPD tests (Fig. 7) were conducted to investigate the oxygen mobility of the catalysts. Zhou et al.[110] reported that doping CeO$_2$ with Pr or Mn causes partial substitution of Ce in the structural cell, resulting in oxygen vacancies and significantly improving O$_2$ desorption at low temperatures. Transition metal CeO$_2$-based catalysts typically have three forms of adsorbed oxygen species: physical or molecular adsorbed species (O$_2^-$), atomic or chemical adsorbed species (O$^-$), and bulk/lattice (O^{2-}), of which peaks are observed at low (below 350 °C), mid and high (above 750 °C) temperatures, respectively.[110] No notable lattice oxygen desorption peaks were seen in the CP alone; however, there were peaks corresponding to chemical and physical-absorbed oxygen ions. The surface oxygen species were generally reduced at temperatures less than 500 °C, while lattice oxygen species were reduced at temperatures greater than 500 °C. It can be noticed that all Mn-doped – CP catalysts have a significant desorption peak of ∼800 °C, related to lattice oxygen species (O^{2-}), atomic/chemical adsorbed oxygen ions at 434 °C (O$^-$), and molecular/physical adsorbed oxygen (O$_2^-$) species at ∼247 °C.

Pure Mn oxide displayed strong desorption peaks related to lattice oxygen species (O^{2-}) at 830 °C. This peak is shifted to the lower temperature of Mn-doped-CP catalysts, indicating

Table 3   H$_2$ TPR and O$_2$ TPD results of Mn$_{(x=5-20)}$(Ce$_{0.9}$Pr$_{0.1}$)O$_{2-\delta}$ catalysts

|	Reduction peak temperature (°C)				Desorption peak temperature (°C)			
	Peak	Peak	Peak	Total H$_2$ consumption	Peak	Peak	Peak	Total O$_2$ desorption
Catalysts	1	2	3	(mmol g^{-1})	1	2	3	(mmol g^{-1})
CP	384 (0.053)	469 (0.203)	548 (0.192)	0.448	402 (0.002)	658 (0.032)	—	0.034
5 Mn-CP	272 (0.287)	448 (0.127)	—	0.414	247 (0.016)	431 (0.021)	759 (0.019)	0.039
10 Mn-CP	274 (0.478)	450 (0.237)	—	0.715	248 (0.009)	441 (0.010)	775 (0.015)	0.034
15 Mn-CP	236 (0.496)	442 (0.355)	—	0.815	252 (0.010)	439 (0.015)	758 (0.037)	0.062
20 Mn-CP	240 (0.792)	428 (0.398)	—	1.190	250 (0.008)	434 (0.017)	745 (0.088)	0.113
Mn oxide	380 (3.831)	492 (11.283)	—	15.11	—	—	831 (0.836)	0.836
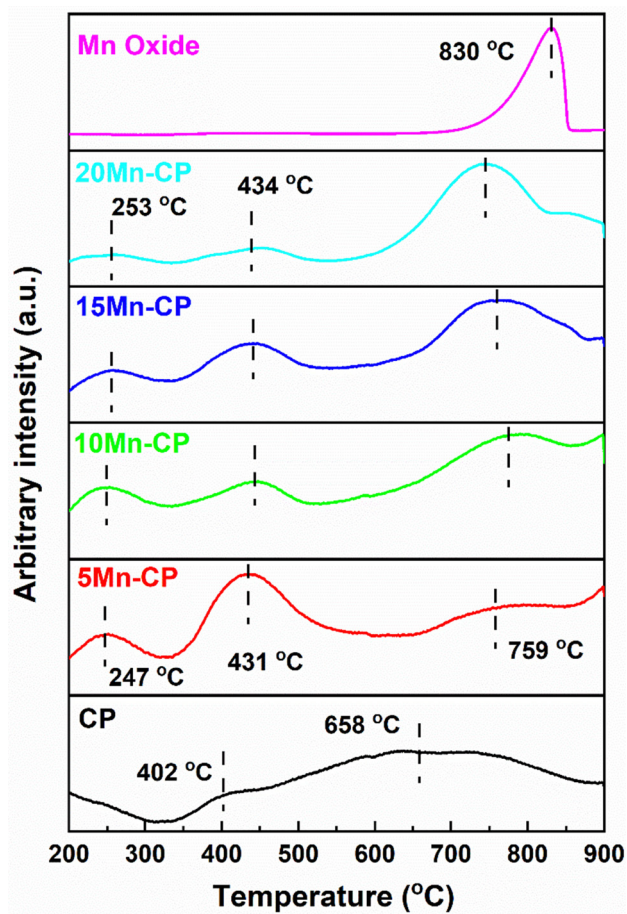
Fig. 7 O_2-TPD profiles of $Mn_{(x=5-20)}(Ce_{0.9}Pr_{0.1})O_{2-\delta}$ catalysts.

enhanced O_2 mobility. Ma et al.[111] reported the desorption peaks at 327, 594, and 654 °C for the Mn-doped Ce catalyst, indicating that it has better oxygen mobility than pure CeO_2 and MnOx. According to Wei et al.,[112] the peak identified between 650 and 850 °C results from the reduction of the internal Ce^{4+} layer and lattice oxygen. Cerium-rich catalysts exhibit enhanced efficacy in transferring oxygen from the lattice to soot surfaces over an extensive temperature range. This is attributable to the elevated mobility of lattice oxygen. Zhao et al.[113] assert that incorporating Ni into Co_3O_4 induces structural distortion, enhances oxygen vacancy density, and augments lattice oxygen mobility. It generates a greater quantity of surface-active oxygen species. The reducibility of a catalyst might signify its capacity to absorb or eliminate oxygen, referred to as the mobility of lattice oxygen, which is frequently linked to catalytic efficacy in soot oxidation.[114]

Soot oxidation typically takes place within the temperature range of 200 to 600 °C, indicating that the medium temperature range associated with active oxygen is crucial. Table 3 provides O_2 desorption at each peak, and it reveals that 5 Mn-CP displayed higher O_2 desorption of 0.037 mmol g^{-1} and 10 Mn-CP displayed low O_2 desorption of 0.019 mmol g^{-1} for surface adsorbed oxygen species, which is consistent with XPS analysis, however, the conditions were different for lattice and bulk oxygen species.

3.3. Soot oxidation activity and activation energy (E_a) determination by the FWO method

Fig. 8 displays the soot conversion curves with the temperature increase. The T_{50} temperature is recorded for each catalyst and is shown in Table 4. The table shows that adding Mn to the CP catalyst system resulted in a considerable drop in T_{50}. Mn-loaded CP catalysts had a higher surface area and T_{50} values ranging from 365 to 395 °C. The T_{50} for the bare CP catalyst was noticed around 408 ± 4 °C,[34] whereas the 5 Mn-CP catalyst had the lowest T_{50} at 365 ± 1 °C, with Mn displaying a higher T_{50} at 433 ± 1 °C. 5-Mn CP has the highest surface area (S_A) of 45 m^2 g^{-1}. Replacing greater ionic radii "Ce" with a smaller ionic radius "Mn" in the fluorite structure would reduce the lattice constant while boosting catalytic activity.[115]

The activation energy (E_a) is determined by plotting Ozawa plots (Fig. S1) and is provided in Table 4. It reveals a modest variance in E_a values and activation energy for Mn-doped Ce catalysts, ranging from 94 to 151 kJ mol^{-1}. Pure Mn oxide (151 ± 3 kJ mol^{-1}) had a somewhat higher E_a value than Mn-doped catalysts. 5 Mn-CP had the lowest E_a value (94 ± 1 kJ mol^{-1}) among all Mn-doped CP catalysts. The uncatalyzed soot oxidation activation energy values range from 150 to 160 kJ mol^{-1}.[4,18] Table 4 also contains existing literature of various Mn-doped Ce-based catalysts synthesized by various techniques and their T_{50} temperatures for soot oxidation reactions. The lowest T_{50} of 298 °C was reported for CeO_2–MnO_2/TiO_2 produced via co-precipitation.[119] CeO_2–MnO_2/TiO_2 exhibits much higher bulk and surface defects, likely because of the CeO_2/TiO_2 interface, which leads to defect formation.[119] Shourya and Dasari[53] reported soot oxidation activity for Mn-doped Ceria, and the improved catalytic activity of $Ce_{0.95}Mn_{0.05}$ was related to its increased surface area, which raises the number of reactive sites. Huang et al.[116] reported that the Ce–Mn crystal structure is more stable, while Mn doping into Ce increases lattice defects, and with increasing Mn concentrations, the oxygen vacancy formation energy decreases. Mukherjee et al.[7] investigated the
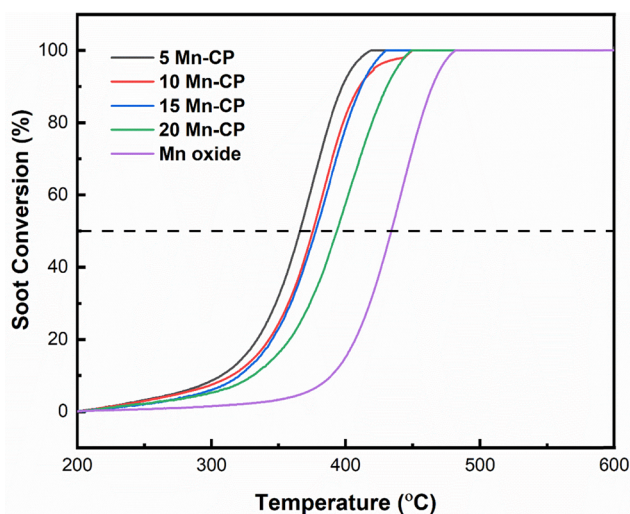

Fig. 8 Soot oxidation activity of $Mn_{(x=5-20)}(Ce_{0.9}Pr_{0.1})O_{2-\delta}$ catalysts.

Table 4 T_{50} and activation energy (E_a) of $Mn_{x(x=0-0.2)}(Ce_{0.9}Pr_{0.1})_{(1-x)}O_{2-\delta}$ catalysts and Mn-doped Ce-based catalysts from the literature

Catalysts	Synthesis method	T_{50} (°C)	E_a (kJ mol^{-1}) FWO method	Ref.
CP	Solution combustion synthesis	408 ± 4	111	This study
5 Mn-CP		365 ± 1	94	
10 Mn-CP		372 ± 2	138	
15 Mn-CP		377 ± 2	143	
20 Mn-CP		395 ± 3	139	
Mn oxide		433 ± 1	151	
$Ce_{0.95}Mn_{0.05}$	EDTA citrate method	360	118	53
$Ce_{0.5}Mn_{0.5}O_2$	Sol–gel method	383	24.86 (Coats–Redfern integral method)	116
Mn doped $Ce_{0.5}Zr_{0.5}O_2$	Incipient wetness impregnation method	360		117
$Ce_{0.95}Mn_{0.05}$	Hydrothermal synthesis	451		118
$Ce_{0.95}Mn_{0.025}Cu_{0.025}$		516		
$CeO_2–MnO_2$	Coprecipitation method	396		119
$CeO_2–MnO_2/TiO_2$		298		
Ceria-manganese	Coprecipitation method	396		7
Ceria-praseodymium		438		
$Ce_{0.9}Pr_{0.1}$	Solid-phase grinding method	398		110
$Ce_{0.9}Mn_{0.1}$		389		
$Ce_{0.9}Pr_{0.1}$	Sol–gel method	414		
$Ce_{0.9}Mn_{0.1}$		399		
Mn-doped ceria	Coprecipitation method	484		120
Mn–Co doped ceria		363		

effect of transition metals (Zr, Hf, Fe, Mn) and rare earth metals (La, Pr) as dopants in Ceria on soot and CO oxidation. Mn doped ceria exhibited better CO and soot oxidation activity, principally due to a significant reduction in lattice oxygen binding energy and a larger concentration of surface adsorbed oxygen species.[7] Zhou et al.[110] reported that the lattice distortion of CeO_2 occurs when Pr is introduced; lattice defects create oxygen vacancies, which aid in the adsorption, movement, and desorption of oxygen. Rao et al.[120] investigated the effect of manganese and cobalt co-doped ceria on soot oxidation activity. Their H_2-TPR analysis revealed that the codoping of ceria remarkably increases the redox behaviour of ceria, as well as surface area and enhanced surface adsorbed oxygen species. Govardhan et al.[86] indicated that Ag/Pr–Ce catalysts exhibit high porosity, which is associated with an increased surface area and pore diameter, enhancing their activity for the oxidation reaction. The elevated concentration of surface Ce^{3+} and the presence of surface chemisorbed oxygen in the 5 Ag/Pr–Ce and 15 Ag/Pr–Ce catalysts played a significant role in enhancing soot oxidation performance. Similarly, the lattice defects and the oxygen vacancies served as crucial descriptors in demonstrating the enhanced soot oxidation activity of the 10 Ni–Pr–Ce catalyst in the studies conducted by Rajvanshi et al.[12] The role of Pr appears to contribute to the enhancement of the catalyst's properties. The inclusion of transition metals further enhances the improved surface parameters.

The descriptors for Ce-based metal oxide that enhance the catalytic performance include the redox ability, the host structure, lattice oxygen species, site isolation, the nature of the metal–oxygen bond, multifunctionality, and phase cooperation.[15] In the case of ceria-based materials, it is not feasible to fixate on a single descriptor; rather, multiple descriptors govern the activity, influenced by the differing reaction conditions. The present investigation demonstrates that the addition of Mn to the Ce–Pr catalyst system improves the catalytic oxidation of soot.

In this study, the catalysts exhibited surface areas varying from 45 to 15 m^2 g^{-1}, with 5 Mn CP demonstrating the highest surface area of 45 m^2 g^{-1}. 5 Mn-CP showed a higher presence of active surface adsorbed species, as demonstrated by XPS and O_2-TPD analysis which influenced catalytic performance displaying the least T_{50} of 365 ± 1 °C. Whereas 10 Mn-CP which had a very slight decrease in T_{50} of 372 ± 2 °C revealed the highest $I_{O_v}/I_{F_{2g}}$ value of 0.78, along with lattice oxygen species as examined through Raman spectroscopy and XPS. CP exhibited a significant reducibility ratio for Ce^{3+}, while the 5 and 10 Mn-CP samples demonstrated a notable concentration of Pr^{3+}. Therefore, the presence of Pr played a significant role in enhancing the Ce^{3+} species on the surface and moderate amounts of Mn enhanced the presence of surface Pr^{3+} ions. Furthermore, the H_2-reduction peaks of 15 Mn-CP and 20 Mn-CP exhibited a shift to lower temperatures, suggesting improved reducibility. Conversely, 20 Mn-CP exhibited the smallest crystallite size along with the largest lattice strain. However, with an increase in the Mn concentration within the Mn-CP catalytic system, a secondary phase emerges, leading to a reduction in activity.

4. Conclusions

$Mn_{x(x=0-0.2)}(Ce_{0.9}Pr_{0.1})_{(1-x)}O_{2-\delta}$ and pure Mn oxide catalysts were effectively produced using the SCS approach. The XRD and Raman analyses demonstrated the fluorite structure of ceria, with the crystallite size for Mn-CP catalysts measured between approximately 5 to 10 nm. 10 Mn-CP exhibited a slightly elevated oxygen vacancy ratio ($I_{O_v}/I_{F_{2g}}$) of 0.78. The catalysts exhibited significant porosity, and the particle size for pure Mn oxide was notably large, as evidenced by the SEM micrographs. The catalysts showed surface areas ranging from 45 to 15 m^2 g^{-1}, with 5 Mn CP displaying the maximum surface

area of 45 m^2 g^{-1}. CP exhibited superior reducibility when compared to all Mn-doped CP catalysts that had a high concentration of Ce^{3+} surface ions. Conversely, 5 Mn-CP exhibited superior active surface adsorbed oxygen species, which are essential for the oxidation of soot. The 5 Mn-CP catalyst demonstrated enhanced catalytic activity, with a T_{50} of 365 $\pm$ 1 °C for the soot oxidation reaction. The factors influencing the soot oxidation activity in the current investigation include surface area, crystallite size, and the presence of active surface adsorbed oxygen species. As the Mn content in the Mn-CP catalytic system rises, a secondary phase emerges, leading to a reduction in soot oxidation activity. 5 Mn-CP showed the lowest activation energy value of 94 kJ mol^{-1} among all the Mn-doped catalysts, whereas Mn$_2$O$_3$ exhibited a slightly higher activation energy value in comparison to the Mn-doped catalysts.

Author contributions

Sunaina S Patil: writing – original draft preparation, review, and editing, resources and methodology, formal analysis, and investigation; Hari Prasad Dasari: conceptualization, formal analysis and investigation, review, supervision, funding acquisition; Rahulkumar Shirasangi: H$_2$-TPR and O$_2$-TPD methodology and investigation. Harshini Dasari: formal analysis investigation, and review.

Data availability

The data can be provided and made available upon request.

Conflicts of interest

The authors declare that they have no conflict of interest.

Acknowledgements

References

1 B. A. A. L. Van Setten, M. Makkee and J. A. Moulijn, *Catal. Rev.: Sci. Eng.*, 2001, **43**, 489–564.

2 M. P. A. Vijay, S. S. Patil, D. R. Madhura, A. P. Anantharaman, P. Gouramma, H. P. Dasari, S. B. Arya and H. Dasari, *Mater. Today: Proc.*, 2022, **57**, 1865–1870.

3 A. P. Anantharaman, H. J. Gadiyar, M. Surendran, A. S. Rao, H. P. Dasari, H. Dasari and G. U. Babu, *Chem. Pap.*, 2018, **72**, 3179–3188.

4 C. S. Shenoy, S. S. Patil, P. Govardhan, A. Shourya and H. P. Dasari, *Emiss. Control Sci. Technol.*, 2019, **5**, 342.

5 S. Ganiger, S. S. Patil, H. P. Dasari, R. Priyanka and S. Kollimarla, *Chem. Eng. Sci.*, 2022, **247**, 117016.

6 L. I. U. Shuang, W. U. Xiaodong, W. Duan and R. A. N. Rui, *J. Rare Earths*, 2015, **33**, 567–590.

7 D. Mukherjee, B. G. Rao and B. M. Reddy, *Appl. Catal., B*, 2016, **197**, 105–115.

8 B. M. Reddy, P. Bharali and G. Thrimurthulu, *Catal. Lett.*, 2008, **123**, 327–333.

9 S. S. Patil, R. Kumar and H. P. Dasari, *J. Taiwan Inst. Chem. Eng.*, 2024, 105459.

10 G. Thrimurthulu, K. N. Rao and D. Devaiah, *et al.*, *Res. Chem. Intermed.*, 2012, **38**, 1847–1855.

11 S. S. Patil, H. Prasad and H. Dasari, *Nano-Struct. Nano-Objects*, 2019, **20**, 100388.

12 K. Rajvanshi, S. S. Patil, Lakhanlal, H. P. Dasari, M. B. Saidutta and H. Dasari, *Chem. Pap.*, 2020, **74**, 4581–4592.

13 S. S. Patil, S. Naik, M. D. Ramesh, H. Dasari and H. P. Dasari, *Chem. Eng. Technol.*, 2022, **45**(3), 517–525.

14 A. P. Anantharaman, H. P. Dasari, H. Dasari and G. U. B. Babu, *Appl. Catal., A*, 2018, **566**, 181–189.

15 R. K. Grasselli, *Top. Catal.*, 2002, **21**, 79–88.

16 Q. Liang, X. Wu, X. Wu and D. Weng, *Catal. Lett.*, 2007, **119**, 265–270.

17 S. Liu, X. Wu, W. Liu, W. Chen, R. Ran, M. Li and D. Weng, *J. Catal.*, 2016, **337**, 188–198.

18 K. Krishna, A. Bueno-López, M. Makkee and J. A. Moulijn, *Appl. Catal., B*, 2007, **75**, 189–200.

19 M. Piumetti, S. Bensaid, N. Russo and D. Fino, *Appl. Catal., B*, 2015, **165**, 742–751.

20 J. Gao, Y. Wang, S. Wang, X. Li, X. Chang, X. Wang, C. Yang and R. Xuan, *Chem. Eng. J.*, 2022, **443**, 136392.

21 E. Aneggi, C. De Leitenburg, G. Dolcetti and A. Trovarelli, *Catal. Today*, 2006, **114**, 40–47.

22 A. Shourya and H. P. Dasari, *Nano-Struct. Nano-Objects*, 2023, **34**, 100970.

23 K. Kim, J. Do Yoo, S. Lee, M. Bae, J. Bae, W. C. Jung and J. W. Han, *ACS Appl. Mater. Interfaces*, 2017, **9**, 15449–15458.

24 Z. Hou, W. Pei, X. Zhang, K. Zhang, Y. Liu, J. Deng and L. Jing, *J. Rare Earths*, 2020, **38**, 819–839.

25 P. Dulgheru and J. A. Sullivan, *Top. Catal.*, 2013, **56**, 504–510.

26 H. P. Dasari, J. S. Ahn, K. Ahn, S. Y. Park, J. Hong, H. Kim, K. J. Yoon, J. W. Son, H. W. Lee and J. H. Lee, *Solid State Ionics*, 2014, **263**, 103–109.

27 H. P. Dasari, S. Y. Park, H.-I. Ji, H.-R. Kim, J.-W. Son, B.-K. Kim, H.-W. Lee and J.-H. Lee, *J. Phys. Chem. C*, 2012, **116**, 3467–3476.

28 T. Vinod Kumar, D. Mukherjee, C. Subrahmanyam and B. M. Reddy, *New J. Chem.*, 2018, **42**, 5276–5283.

29 A. Hernández-Giménez A, L. Xavier and A. Bueno-López, *Appl. Catal., A*, 2013, **462–463**, 100–106.

30 D. N. Durgasri, T. Vinodkumar, F. Lin, I. Alxneit and B. M. Reddy, *Appl. Surf. Sci.*, 2014, **314**, 592–598.

31 P. Sudarsanam, K. Kuntaiah and B. M. Reddy, *New J. Chem.*, 2014, **38**, 5991–6001.

32 A. P. Anantharaman, J. Geethu, M. R. Rahul, H. P. Dasari and H. Dasari, *Mol. Catal.*, 2018, **451**, 247–254.

33 E. Aneggi, C. De Leitenburg, G. Dolcetti and A. Trovarelli, *Top. Catal.*, 2007, **42–43**, 319–322.

34 S. S. Patil and H. P. Dasari, *Braz. J. Chem. Eng.*, 2023, **41**, 269–285.

35 S. S. Patil and H. P. Dasari, *Environ. Sci. Pollut. Res.*, 2024, DOI: 10.1007/s11356-024-35652-1.

36 M. Machida, Y. Murata, K. Kishikawa, D. Zhang and K. Ikeue, *Chem. Mater.*, 2008, **20**, 4489–4494.

37 T. Vinodkumar, D. Durgasr Naga and B. M. Reddy, *Int. J. Adv. Eng. Sci.*, 2013, **5**, 224–231.

38 A. A. Khaskheli, L. Xu and D. Liu, *Energy Fuels*, 2022, **36**(4), 7219–7920.

39 Q. Liang, X. Wu, D. Weng and H. Xu, *Catal. Today*, 2008, **139**, 113–118.

40 S. K. Ghosh, *ACS Omega*, 2020, **5**, 25493–25504.

41 M. Fu, J. Lin, W. Zhu, J. Wu, L. Chen, B. Huang and D. Ye, *J. Rare Earths*, 2014, **32**, 153–158.

42 S. D. Neelapala, A. Shetty, G. Gaggar, R. Mall and H. Dasari, *Int. J. Appl. Eng. Res.*, 2018, **13**, 245–251.

43 Y. Kuwahara, G. Kato, A. Fujibayashi, K. Mori and H. Yamashita, *Chem. – Asian J.*, 2020, **15**, 2005–2014.

44 P. Venkataswamy, D. Jampaiah, D. Mukherjee, C. U. Aniz and B. M. Reddy, *Catal. Lett.*, 2016, **146**, 2105–2118.

45 H. Zhang, J. Wang, Y. Cao, Y. Wang, M. Gong, Y. Chen and C. Xuebao, *Chin. J. Catal.*, 2015, **36**, 1333–1341.

46 X. Yue, D. Ye, M. Fu, J. Wu, J. Ouyang, B. Huang and H. Liang, *Catal. Today*, 2010, **153**, 125–132.

47 A. B. Aberkane, M. P. Yeste, D. Fayçal, D. Goma and M. Á. Cauqui, *Materials*, 2019, **12**(20), 3436.

48 X. Niu, M. Li, B. Hao and H. Li, *J. Mater. Sci.:Mater. Electron.*, 2016, **27**, 6845–6848.

49 P. Palmisano, N. Russo, P. Fino, D. Fino and C. Badini, *Appl. Catal., B*, 2006, **69**(1–2), 85–92.

50 S. Patil and H. P. Dasari, *Mater. Sci. Energy Technol.*, 2019, **2**, 485–489.

51 I. Shajahan, J. Ahn, P. Nair, S. Medisetti, S. Patil, V. Niveditha, G. Uday Bhaskar Babu, H. P. Dasari and J. H. Lee, *Mater. Chem. Phys.*, 2018, **216**, 136–142.

52 A. J. Zarur and J. Y. Ying, *Nat. Lett.*, 2000, **403**, 65–67.

53 A. Shourya and H. P. Dasari, *Chem. Pap.*, 2022, **76**(11), 7095–7110.

54 A. P. Anantharaman, H. P. Dasari, J. H. Lee, H. Dasari and G. U. B. Babu, *Catal. Lett.*, 2017, **147**, 3004–3016.

55 E. Kumar, P. Selvarajan and D. Muthuraj, *Mater. Res.*, 2013, **16**, 269–276.

56 A. Varma, A. S. Mukasyan, A. S. Rogachev and K. V. Manukyan, *Chem. Rev.*, 2016, **116**, 14493–14586.

57 A. Varma and A. S. Mukasyan, *Korean J. Chem. Eng.*, 2004, **21**, 527–536.

58 T. Ozawa, *Thermochim. Acta*, 1992, **203**, 159–165.

59 B. M. Reddy, G. Thrimurthulu and L. Katta, *Catal. Lett.*, 2011, **141**, 572–581.

60 E. Aneggi, D. Wiater, C. De Leitenburg, J. Llorca and A. Trovarelli, *ACS Catal.*, 2014, **4**, 172–181.

61 A. S. Ryabova, S. Y. Istomin, K. A. Dosaev, A. Bonnefont, J. Hadermann, N. A. Arkharova, A. S. Orekhov, R. P. Sena, V. A. Saveleva, G. Kéranguéven, E. V. Antipov, E. R. Savinova and G. A. Tsirlina, *Electrochim. Acta*, 2020, 137378.

62 X. Niu, H. Wei, K. Tang, W. Liu, G. Zhao and Y. Yang, *RSC Adv.*, 2015, **5**, 66271–66277.

63 B. C. Yadav, M. Singh and C. D. Dwivedi, *Sens. Transducers J.*, 2011, **125**(2), 68–75.

64 R. Lo Nigro, R. G. Toro, G. Malandrino, V. Raineri and I. L. Fragalà, *Adv. Mater.*, 2003, **15**(3), 1071–1075.

65 M. Shiraishi and M. Inagaki, *Carbon Alloys*, 2003, **10**, 161–173.

66 H. Chi, P. Zhang, J. Xiong, Y. Wei, Y. Li and Z. Zhao, *Appl. Surf. Sci.*, 2023, **608**, 155116.

67 E. Aneggi, C. de Leitenburg, J. Llorca and A. Trovarelli, *Catal. Today*, 2012, **197**, 119–126.

68 H. Zhao, X. Zhou, M. Wang, Z. Xie, H. Chen and J. Shi, *RSC Adv.*, 2017, **7**, 3233–3239.

69 J. G. Kang, B. K. Min and Y. Sohn, *J. Alloys Compd.*, 2015, **619**, 165–171.

70 T. S. Soliman, S. I. Elkalashy and M. M. Hessien, *J. Mater. Sci.: Mater. Electron.*, 2024, **35**, 2083.

71 R. Naeem, M. Ali Ehsan, R. Yahya, M. Sohail, H. Khaledi and M. Mazhar, *Dalton Trans.*, 2016, **45**, 14928–14939.

72 Y. Xin, H. Cao, C. Liu, J. Chen, P. Liu, Y. Lu and Z. Ling, *J. Raman Spectrosc.*, 2022, **53**, 340–355.

73 I. El Arrouji, C. Chen, J. Toyir, C. Larabi, K. C. Szeto, A. de Mallmann, M. Taoufik and A. Oulmekki, *Catalysts*, 2021, **11**(8), 950.

74 M. AlKetbi, K. Polychronopoulou, M. Abi Jaoude, M. A. Vasiliades, V. Sebastian, S. J. Hinder, M. A. Baker, A. F. Zedan and A. M. Efstathiou, *Appl. Surf. Sci.*, 2020, **505**, 144474.

75 R. Kumar, *Surface Characterization Techniques*, 2022, ISBN 978-3-11-065599-5.

76 J. C. Groen, L. A. A. Peffer and J. Pérez-Ramírez, *Micro-porous Mesoporous Mater.*, 2003, **60**, 1–17.

77 S. Yang, J. Wang, W. Chai, J. Zhu and Y. Men, *Catal. Sci. Technol.*, 2019, **9**, 1699–1709.

78 S. T. Aruna and A. S. Mukasyan, *Curr. Opin. Solid State Mater. Sci.*, 2008, **12**, 44–50.

79 T. Drake, P. Ji and W. Lin, *Acc. Chem. Res.*, 2018, **51**, 2129–2138.

80 M. Mittal, A. Gupta and O. P. Pandey, *Sol. Energy*, 2018, **165**, 206–216.

81 S. Hassan, R. Kumar, A. Tiwari, W. Song, L. van Haandel, J. K. Pandey, E. Hensen and B. Chowdhury, *Mol. Catal.*, 2018, **451**, 238–246.

82 J. P. Holgado, R. Alvarez and G. Munuera, *Appl. Surf. Sci.*, 2000, **161**, 301–315.

83 A. S. Diez, M. Graziano-Mayer, G. Radivoy and M. A. Volpe, *Appl. Catal., A*, 2014, **482**, 24–30.

84 C. Li, Y. Sun and A. Zhang, *RSC Adv.*, 2015, **5**, 36394–36403.

85 E. Poggio-Fraccari, G. Baronetti and F. Mariño, *J. Electron Spectrosc. Relat. Phenom.*, 2018, **222**, 1–4.

86 P. Govardhan, A. P. Anantharaman, S. S. Patil, H. P. Dasari, H. Dasari and A. Shourya, *Korean J. Chem. Eng.*, 2022, **39**, 328–342.

87 J. F. Moulder, W. F. Stickle, P. E. Sobol and K. D. Bomben, *Handbook of X-ray Photoelectron Spectroscopy*, 1992, ISBN: 0-9627026-2-5.

88 N. Paunović, Z. Dohcevic-Mitrovic, R. Scurtu, S. Aškrabić, M. Prekajski, B. Matović and Z. V. Popović, *Nanoscale*, 2012, **4**, 5469–5476.

89 M. Wang, K. Chen, J. Liu, Q. He, G. Li and F. Li, *Catalysts*, 2018, **8**(4), 138.

90 R. Patel, A. H. Fakeeha, S. O. Kasim, M. L. Sofiu, A. A. Ibrahim, A. E. Abasaeed, R. Kumar and A. S. Al-Fatesh, *Mol. Catal.*, 2021, **510**, 111676.

91 A. S. Al-Fatesh, R. Kumar, S. O. Kasim, A. A. Ibrahim, A. H. Fakeeha, A. E. Abasaeed, R. Alrasheed, A. Bagabas, M. L. Chaudhary, F. Frusteri and B. Chowdhury, *Catal. Today*, 2020, **348**, 236–242.

92 N. Paunović, Z. Dohčević-Mitrović, R. Scurtu, S. Aškrabić, M. Prekajski, B. Matović and Z. V. Popović, *Nanoscale*, 2012, **4**(17), 5469–5476.

93 T. E. Jones, T. C. R. Rocha, A. Knop-Gericke, C. Stampfl, R. Schlögl and S. Piccinin, *ACS Catal.*, 2015, **5**, 5846–5850.

94 J. He, T. Wang, X. Bi, Y. Tian, C. Huang, W. Xu, Y. Hu, Z. Wang, B. Jiang, Y. Gao, Y. Zhu and X. Wang, *Nat. Commun.*, 2024, **15**, 5422.

95 T. E. Jones, T. C. R. Rocha, A. Knop-Gericke, C. Stampfl, R. Schlögl and S. Piccinin, *ACS Catal.*, 2015, **5**, 5846–5850.

96 L. V. Yafarova, G. V. Mamontov, I. V. Chislova, O. I. Silyukov and I. A. Zvereva, *Catalysts*, 2021, **11**(10), 1256.

97 V. Dimitrov, T. Komatsu and R. Sato, *J. Ceram. Soc. Jpn.*, 1999, **107**(1241), 21–26.

98 D. N. G. Krishna and J. Philip, *Appl Surf. Sci. Adv.*, 2022, **12**, 100332.

99 M. Kantcheva, M. U. Kucukkal and S. Suzer, *J. Mol. Struct.*, 1999, **482–483**, 19–22.

100 P. Sudarsanam, K. Kuntaiah and B. M. Reddy, *New J. Chem.*, 2014, **38**, 5991–6001.

101 Y. Wei, J. Liu, Z. Zhao, A. Duan, G. Jiang, C. Xu, J. Gao, H. He and X. Wang, *Energy Environ. Sci.*, 2011, **4**, 2959–2970.

102 J. Chen, X. Chen, X. Chen, W. Xu, Z. Xu, H. Jia and J. Chen, *Appl. Catal., B*, 2018, **224**, 825–835.

103 N. Guillén-Hurtado, J. Giménez-Mañogil, J. C. Martínez-Munuera, A. Bueno-López and A. García-García, *Appl. Catal., A*, 2020, **590**, 117339.

104 A. Jan, J. Shin, J. Ahn, S. Yang, K. J. Yoon, J. W. Son, H. Kim, J. H. Lee and H. Il Ji, *RSC Adv.*, 2019, **9**, 27002–27012.

105 J. He, H. Zhang, W. Wang, P. Yao, Y. Jiao, J. Wang and Y. Chen, *Environ. Sci. Pollut. Res.*, 2021, **28**, 26018–26029.

106 A. S. Nayak, S. S. Patil, H. P. Dasari, D. Telaginatot, M. Rynjah and S. Cheruku, *Chem. Eng. Res. Des.*, 2024, **208**, 910–920.

107 J. Zhang, Y. Li, L. Wang, C. Zhang and H. He, *Catal. Sci. Technol.*, 2015, **5**, 2305–2313.

108 P. Gong, J. Xie, D. Fang, F. He, F. Li and K. Qi, *Mater. Res. Express*, 2017, **4**, 115036.

109 L. Fan, K. Xi, Y. Zhou, Q. Zhu, Y. Chen and H. Lu, *RSC Adv.*, 2017, **7**, 20309–20319.

110 B. Zhou, K. Xi, L. J. Fan, Y. Zhou, Y. Wang, Q. L. Zhu and H. F. Lu, *Appl. Catal., A*, 2018, **562**, 1–10.

111 J. Ma, X. Li, C. Zhang, Q. Ma and H. He, *Appl. Catal., B*, 2020, **264**, 118498.

112 Y. Wei, J. Liu, Z. Zhao, A. Duan and G. Jiang, *J. Catal.*, 2012, **287**, 13–29.

113 M. Zhao, J. Deng, J. Liu, Y. Li and J. Liu, *et al.*, *Catalysis*, 2019, **9**(8), 7548–7567.

114 P. Yao, J. He, X. Jiang, Y. Jiao, J. Wang and Y. Chen, *J. Energy Inst.*, 2020, **93**, 774–783.

115 X. Wu, S. Liu, D. Weng, F. Lin and R. Ran, *J. Hazard. Mater.*, 2011, **187**, 283–290.

116 H. Huang, J. Liu, P. Sun, S. Ye and B. Liu, *RSC Adv.*, 2017, **7**, 7406–7412.

117 J. He, P. Yao, J. Qiu, H. Zhang, Y. Jiao, J. Wang and Y. Chen, *Fuel*, 2021, **286**, 119359.

118 M. Dosa, M. Piumetti, S. Bensaid, T. Andana, C. Novara, F. Giorgis, D. Fino and N. Russo, *Catal. Lett.*, 2018, **148**, 298–311.

119 D. Mukherjee, P. Venkataswamy, D. Devaiah, A. Rangaswamy and B. M. Reddy, *Catal. Sci. Technol.*, 2017, **7**, 3045–3055.

120 B. Govinda Rao, D. Jampaiah, P. Venkataswamy and B. M. Reddy, *ChemistrySelect*, 2016, **1**, 6681–6691.